Monitoring mouse retinal degeneration with high-resolution spectral-domain optical coherence tomography

Ki Hean Kim
Wellman Center for Photomedicine, Massachusetts General Hospital, Boston, MA, USA

Mehron Puoris'haag
Wellman Center for Photomedicine, Massachusetts General Hospital, Boston, MA, USA

Gopi N. Maguluri
Wellman Center for Photomedicine, Massachusetts General Hospital, Boston, MA, USA

Yumiko Umino
Center for Vision Research, SUNY Upstate Medical University, Syracuse, NY, USA

Karen Cusato
Center for Vision Research, SUNY Upstate Medical University, Syracuse, NY, USA

Robert B. Barlow
Center for Vision Research, SUNY Upstate Medical University, Syracuse, NY, USA

Johannes F. de Boer
Wellman Center for Photomedicine, Massachusetts General Hospital, Boston, MA, USA

Progression of retinal degeneration in a mouse model was studied *in vivo* with high-resolution spectral-domain optical coherence tomography (SD-OCT). Imaging in 3D with high depth resolution (<3 μm), SD-OCT resolved all the major layers of the retina of control C57BL/6J mice. Images of transgenic mice having a null mutation of the rhodopsin gene revealed the anatomical consequences of retinal degeneration: thinning of the outer retina, including the outer plexiform layer (OPL), outer nuclear layer (ONL), and inner and outer segments (IS/OS). We monitored the progression of retinal degeneration in *rd*1 mice (C3H/HeJ) by periodically imaging the same mice from the time the pups opened their eyes on P13 to P34. SD-OCT images showed that the outer retina (OPL, ONL, IS/OS) had already thinned by 73% (100 to 27 μm) at eye opening. The retina continued to degenerate, and by P20 the outer retina was not resolvable. The thickness of entire retina decreased from 228 μm (control) to 152 μm on P13 and to 98 μm by P34, a 57% reduction with the complete loss in the outer retina. In summary, we show that SD-OCT can monitor the progression of retinal degeneration in transgenic mice.

Keywords: spectral-domain optical coherence tomography, imaging, mouse model, retinal degeneration

Citation: Kim, K. H., Puoris'haag, M., Maguluri, G. N., Umino, Y., Cusato, K., Barlow, R. B., & de Boer, J. F. (2008). Monitoring mouse retinal degeneration with high-resolution spectral-domain optical coherence tomography. *Journal of Vision, 8*(1):17, 1–11, http://journalofvision.org/8/1/17/, doi:10.1167/8.1.17.

Introduction

Rodent models are powerful tools for retinal degeneration studies including detecting gene defects and understanding cellular pathways and molecular mechanisms underlying degeneration. Mouse models are especially valuable with the availability of the genome database and ease of genetic manipulation. Many mouse models are currently available and more are being developed to study a variety of retinal

doi: 10.1167/8.1.17 Received March 28, 2007; published January 24, 2008 ISSN 1534-7362

degenerative diseases (Chang et al., 2002). They also have proven useful in developing treatment methods such as gene therapy and stem cell therapy. Various gene therapy methods have been developed to stop retinal degeneration resulting from gene defects or to treat related disorders involving angiogenesis and inflammation (Alexander et al., 2007; Ali et al., 2000; Bainbridge, Tan, & Ali, 2006; Hauswirth & Beaufrere, 2000). Recent advances in stem cell research have demonstrated rescue of cones in the mouse retina (Otani et al., 2004).

The advance of optical imaging techniques has aided retinal degeneration research in animal models by providing visualization of 3D structures at the cellular level in vivo (Morgan, Huckfeldt, & Wong, 2005). One emerging in vivo imaging technique is optical coherence tomography (OCT) that produces cross-sectional images of tissue structures non-invasively based on its optical reflectivity, analogous to ultrasound (Fujimoto, 2003; Huang et al., 1991). In 2001 the time domain optical coherence tomography (TD-OCT) was used to study mouse models of retinal degeneration (Horio et al., 2001; Li et al., 2001). TD-OCT was able to resolve thinning of the mouse retina, but the low depth resolution (17 μm) of the used systems precluded resolution of detailed retinal microstructures. Advances in OCT technology have enabled high-resolution, high-speed imaging. A higher depth resolution of 3 μm can be achieved using broadband light sources (Drexler et al., 2001). A new method, the so-called Fourier domain or spectral-domain OCT (FD-, SD-OCT) (Hausler & Lindner, 1998; Wojtkowski, Leitgeb, Kowalczyk, Bajraszewski, & Fercher, 2002), can image 10–100 times faster than TD-OCT without loss of image quality (Cense et al., 2004; de Boer et al., 2003; Leitgeb, Hitzenberger, & Fercher, 2003; Nassif et al., 2004; Wojtkowski et al., 2004). High-resolution SD-OCT systems could rapidly acquire 3D images resolving the microstructures of the rodent retina (Ruggeri et al., 2007; Srinivasan, Ko, et al., 2006). Srinivasan, Wojtkowski, Fujimoto, and Duker (2006) used high-resolution SD-OCT to study light-induced changes of optical properties (scattering) of the outer segment in the rat retina.

In this study, we developed a high-resolution SD-OCT system capable of resolving the layered microstructures of the mouse retina. We used the system to study retinal degeneration in *rd*1 mice. Retinal degeneration in *rd*1 mice is caused by a null mutation of the rhodopsin gene (Bowes et al., 1993). We report here that the high-resolution SD-OCT system can monitor the progressive anatomical changes in the retinas of individual *rd*1 mice and detect the time-dependent thinning of retinal layers that occurs during the first month of life.

Materials and methods

System setup

A simple schematic of our SD-OCT system is presented in Figure 1. The system is a fiber-based interferometer. The light source is a broadband Ti:sapphire laser (Femto-Lasers, Austria) which provides a 110-nm bandwidth at the sample arm after fiber coupling of the laser source at 800-nm center wavelength. This broadband light source provides an axial (depth) resolution of less than 3 μm in tissue (Swanson et al., 1992). Light is divided at a fiber coupler (AC Photonics, Santa Clara, CA), which has an 80:20 splitting ratio, into two paths: the reference arm (80%) and the sample arm (20%). The reference arm is based on a simple reflector and provides the reference optical path length. The sample arm is designed for imaging small mouse eyes: Light from the fiber is collimated, reflected by galvanometric mirror scanners (Cambridge Technology, Watertown MA), and relayed to

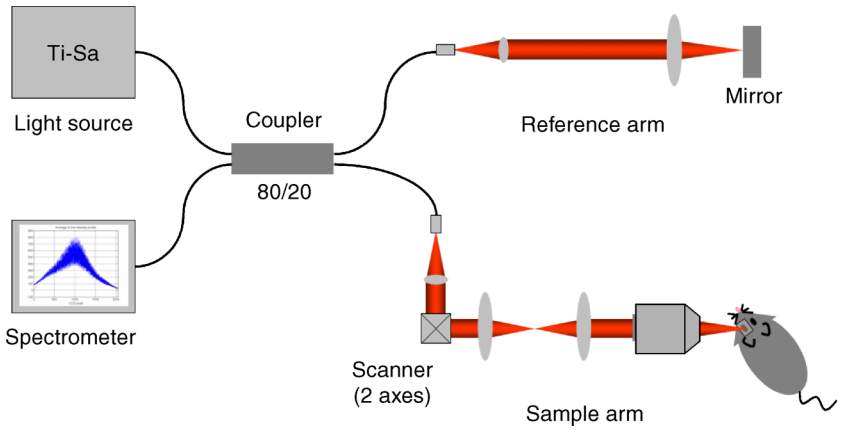

Figure 1. Schematic of the high-resolution SD-OCT system for mouse retinal imaging. The system is based on a fiber coupler. Broadband light from the Ti-Sa laser is split into both the reference arm and sample arm. Back-scattered light from the retina is coupled back to the fiber, combined with reflected light from the reference arm at the coupler, and delivered to the spectrometer. Light in the air is depicted in red.

an objective (EC Plan-Neofluar 5×, 13.6 mm WD 0.15 NA, Zeiss, NJ) via a lens pair (150 mm focal length). The objective focuses light onto the retina of an anesthetized mouse. The refractive power of the mouse eye is largely negated by applying hydroxypropyl methylcellulose (Methocel® 2%, Excelvision, Annonay, France) and gently placing a coverslip on the eye (Srinivasan, Ko, et al., 2006). This method effectively removes the refractive power of the air-corneal interface. In addition, this method prevents the cornea from dehydration and reduces the risk of cataract formation. The objective is corrected for chromatic aberration, which is necessary because of the broad bandwidth of the light source. The *x*–*y* scanners move the focused light across the retina in the lateral plane.

Back-scattered light from the retina is collected by the objective and delivered to the fiber coupler where it is combined with reflected light from the reference arm. The combined light generates interference by matching traveling path lengths in both the reference and sample arms. The generated interference is spectrally resolved and detected by a custom made spectrometer in the detection arm (Nassif et al., 2004). The acquired spectrum is numerically interpolated to the *k*-space (2π/wavelength) (Wojtkowski et al., 2002). Fourier transforming the interpolated spectrum yields a depth reflectivity profile (*z*) (Fercher, Hitzenberger, Kamp, & El-Zaiat, 1995). This process is repeated for the spectral interferogram at each lateral position (*x, y*) during the beam scanning. Dispersion imbalance between the sample and reference arms, resulting from more optical elements in the sample than in the reference arm, reduces axial resolution. We measure this dispersion imbalance during calibration by placing a reflector in the sample arm, compensating for it numerically in the signal processing (Cense et al., 2004; Wojtkowski et al., 2004). The objective has a numerical aperture (NA) of 0.15, and the NA of the focusing beam onto the eye is reduced to 0.05 by underfilling the back-aperture of the objective. This gives a 400-μm depth of focus that is large enough to keep light being focused through the thickness of the retina. The 0.05 NA yields a theoretical image resolution of 6 μm in the lateral plane (*x*–*y*). We measured the actual resolution by imaging 2 μm diameter polymer microspheres (4202A, Duke Scientific co., Fremont, CA) as point sources. The microspheres were immobilized and sparsely distributed in agar gel. We found that the full width at half maximum intensity (FWHM) in the *x*–*y* plane averaged 6 μm (n = 10), which matched well the theoretical value. We measured depth resolution by imaging a mirror as the sample and found the FWHM to be 3.0 μm (on average) in air.

Imaging the mouse retina

Mice were anesthetized with Pentobarbital (Nembutal®, Ovation Pharmaceuticals, Inc., Deerfield, IL) 50 mg/kg body weight applied i.p. The eye pupils were dilated with drops of Tropicamide Ophthalmic Solution USP 1% (Bausch & Lomb Inc., Tampa, FL). Hydroxypropyl methylcellulose (Methocel® 2%) and microscopic coverslips were applied onto the eyes as mentioned in the previous section. During imaging, the mouse was placed in a holder and temperature was controlled with heating pads adjusted to approximately 33°C. 3D SD-OCT imaging was performed on two regions of each eye using the optic nerve head as a landmark: one on the nasal side of the optic nerve head and the other on the temporal side. The optical power delivered to the eye was approximately 1.2 mW, which is twice the maximum power for imaging the human eye with a stationary beam according to the ANSI standard (American National Standards Institute, 2000). We assumed that twice the maximum power would be also safe when using a scanning beam. This twice input power increased the signal by a factor of 2 (3 dB). In SD-OCT, a single spectrum measurement provided a depth reflectivity profile (or depth scan) of the retina at the location of the illuminating beam. Using common coordinates, we assigned the depth direction to the *z* axis and the lateral direction to the *x*–*y* plane. A cross-sectional image (in the *x*–*z* plane) was constructed from consecutive depth scans with the beam scanning in one lateral direction (*x*). The lateral scanning range was limited by the pupil and measured from 1.2 mm to 1.8 mm depending on age and strain. Each cross-sectional image was composed of 1000 consecutive depth scans, and individual depth scans had 1024 pixels covering a depth range of 1.8 mm in tissue (1000 × 1024 pixels in *x*–*z* plane). Following this procedure, we acquired a 3D image set from consecutive cross-sectional images by slow scanning the beam in the y axis. Since the retina was thinner than the depth range of cross-sectional images (1.8 mm in tissue), the images were cropped in the *z* axis from 1024 to 384 pixels to cover 0.67 mm. The SD-OCT system acquired 29,000 depth scans/s and this speed corresponded to 29 frames/s for the cross-sectional images composed of 1000 depth scans/frame. For typical retinal images, the dynamic range was approximately 42 dB, defined as the ratio of maximum signal over noise floor. Both the maximum signal and noise floor pertained to cross-sectional images of the retina. The noise floor was an average signal level of background (outside of the retina) in the images. All animal procedures were performed with a protocol approved by the Committee on Animal Care at Massachusetts General Hospital.

Histology

Mice were euthanized, at multiple time points, with Pentobarbital 200 mg/kg i.p. and eyeballs were enucleated. Before enucleation, the posterior edge of the cornea was scarred with a hot needle as an orientation marker. The eyeballs were carefully enucleated and stored in formalin. They were then postfixed in 1% OsO_4/2%

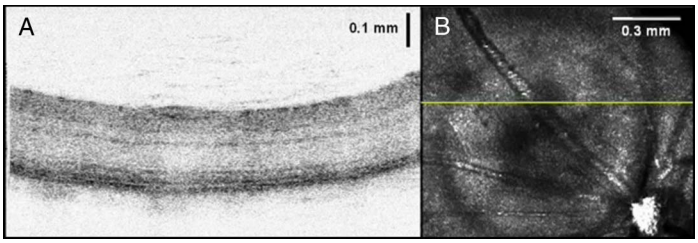

Movie 1. High-resolution SD-OCT images of a control mouse retina (C57BL/6J, P50). (a) Movie of cross-sectional images, (b) fundus image generated from the 3D cross-sectional images. The cross-sectional image advances with 6 μm step size and visualizes layered microstructures of the retina. The cross-sectional line is depicted in the fundus image.

paraformaldehyde/1.25% glutaraldehyde in PBS for 1 hour, dehydrated, and then embedded in epoxy resin following standard protocol. Vertical sections (1 μm in thickness) were cut through the center of the eye and stained with toluidine blue for light microscopy.

Results

Comparing SD-OCT images of normal mouse retina with histology

We first imaged control mice (C57BL/6J, 50 days old) to test our imaging system. Since eyes of the mice at this age were small, scanning dimensions were 1.2 mm $\times$ 1.0 mm in the x–y plane. The consecutive cross-sectional images were processed as a movie and presented in Movie 1. These cross-sectional images are displayed in an inverse gray scale such that black corresponds to highest intensity level and white to lowest level. A fundus image in Movie 1 was constructed from the 3D SD-OCT image set by summing intensities in the z axis and is displayed in a gray scale with white corresponding to highest intensity and black to lowest intensity. The cross-sectional images show layered retinal microstructures because individual layers have different scattering properties with slightly different refractive indices. These retinal microstructures are better resolved in the central than in the peripheral regions of the 3D image because the focus of light degrades in the periphery (see Discussion). Large blood vessels appear close to the inner surface of the retina and cause weak signal shadows below them in the cross-sectional images. These shadows result from absorption and scattering of light by the blood vessels. The fundus image displays the blood vessels branching from the optic nerve head on the lower right corner.

We identified individual retinal layers in SD-OCT images (Figure 2b) by comparing them with histological images (Figure 2a) from the same retina. An SD-OCT image strip was extracted at around 0.5 mm to the side of the optic nerve head and resized to roughly match the histological image. From the top (proximal) surface of the retina to the bottom (distal), the nerve fiber layer (NFL) and ganglion cell layer (GCL) appear together as a dark thin band with strong light scattering. The GCL is not distinguished from the NFL. The inner plexiform layer (IPL) is apparent as a thick band of intermediate intensity just below the NFL/GCL. The inner nuclear layer (INL)

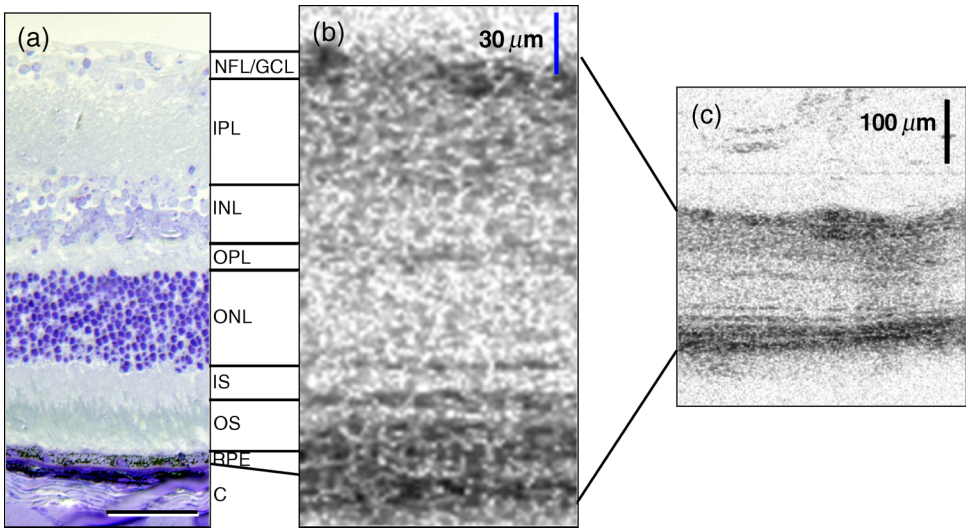

Figure 2. Comparison between a high-resolution SD-OCT image of the control mouse retina and a histological image of the same retina. The SD-OCT image shows all the major retinal layers in good correlation with histology. The scale bar in the histological image is 50 μm.

appears as a light band and the outer plexiform layer (OPL) appears as a thin strip with intensity similar to the IPL. The outer nuclear layer (ONL) appears as a light thick band. Both nuclear layers scatter light weakly and appear light gray, and both plexiform layers scatter light strongly and appear darker gray. The outer limiting membrane (OLM) is located distal to the ONL along the length of the IS. The OLM is comprised of the distal terminations of Müller cells. The OLM surface facing the RPE is expanded by many small projections called apical villi. These villi together with the OLM itself seem to strongly scatter light and appear as a dark line in the image. The junction between the IS and OS is also visible as a dark line. The strong light scattering may result from the transition from the mitochondrial-containing ellipsoid in the IS to the OS (Gloesmann et al., 2003) or from the transition from the IS to the OS which has a high protein density in tightly stacked membrane discs. The RPE and the choroid appear as dark lines below. The RPE line appears thick possibly because of strong light scattering by high protein density at the tip of the OS. This labeling is in general agreement with previous reports (Ruggeri et al., 2007; Srinivasan, Ko, et al., 2006).

We reconstructed a 3D retinal image of a control mouse (C57BL/6J, 5 months old) from consecutive cross-sectional images using a commercial software (Amira, Mercury Computer Systems) in Figure 3. The image dimensions were 1.8 mm × 1.2 mm × 0.67 mm in the *x*, *y*, and *z* axes. This 3D image was displayed in an inverse-gray scale, and the transparency of image pixels was adjusted such that the lighter gray (lower intensity) pixels became more transparent. This adjustment enhanced visibility of small connected structures below the inner surface in the top view of the 3D retinal image (arrow in Figure 3a), which we believe to be vasculature. An empty region in the middle of the top view image was due to lack of signal because light was scattered or absorbed by other eye structures including the cornea and lens before reaching the retina. A side view (Figure 3b) shows the optic nerve head protruding from the inner surface of the retina. This 3D rendering demonstrates that high-resolution SD-OCT can elucidate microstructures of the mouse retina in 3D.

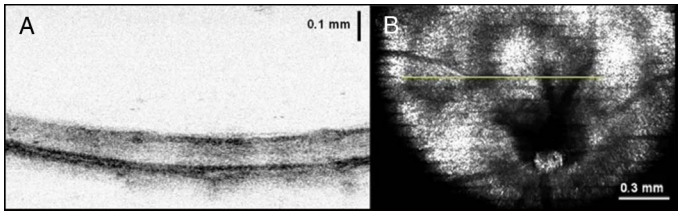

Movie 2. A high-resolution SD-OCT image of a rhodopsin knockout mouse retina (8 month old). (a) A movie of cross-sectional images, (b) a fundus image generated from the 3D cross-sectional images. Not many layers are present in the retina due to the retinal degeneration.

Comparing SD-OCT images of rhodopsin knockout mouse retina with histology

We next imaged retinas from mice having a null mutation of the rhodopsin gene that leads to degeneration of the photoreceptor layer (Lem et al., 1999). The mice imaged were 8 months old by which time the retinal degeneration was complete. Consecutive cross-sectional images were acquired for a 3D image set, and its dimensions were 1.8 mm × 1.2 mm × 0.67 mm in the *x*, *y*, and *z* axes. Movie 2 presents consecutive cross-sectional images and a fundus image generated by the same method used for the control mouse. In the movie, the cross-sectional images were cropped in the *x* axis from 1.8 mm to 1.2 mm. The fundus image was constructed from the cross-sectional images without cropping and its dimensions were 1.8 mm × 1.2 mm in the *x*–*y* plane. The cross-sectional images show that the retina is thinner and has fewer distinguishable layers than the control. The small motion of the retina in the movie is caused by the

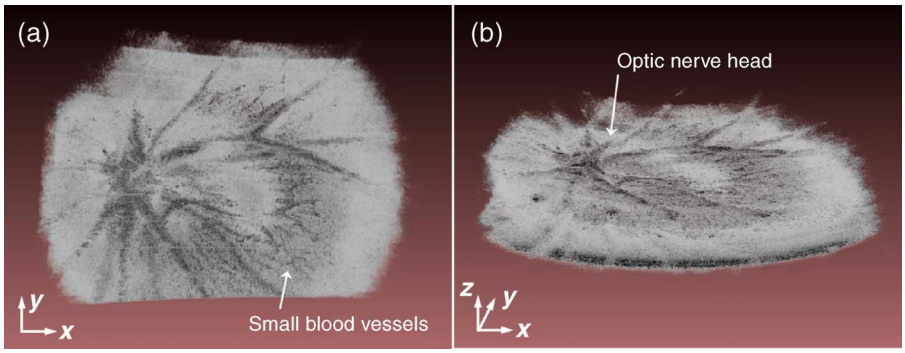

Figure 3. 3D rendering of control mouse retina (C57BL/6J) in top view (a) and side view (b). Dimensions of the volume are 1.8 mm × 1.2 mm × 0.67 mm in the *x*, *y*, and *z* axes. The blood vessel network is visible in the top view.

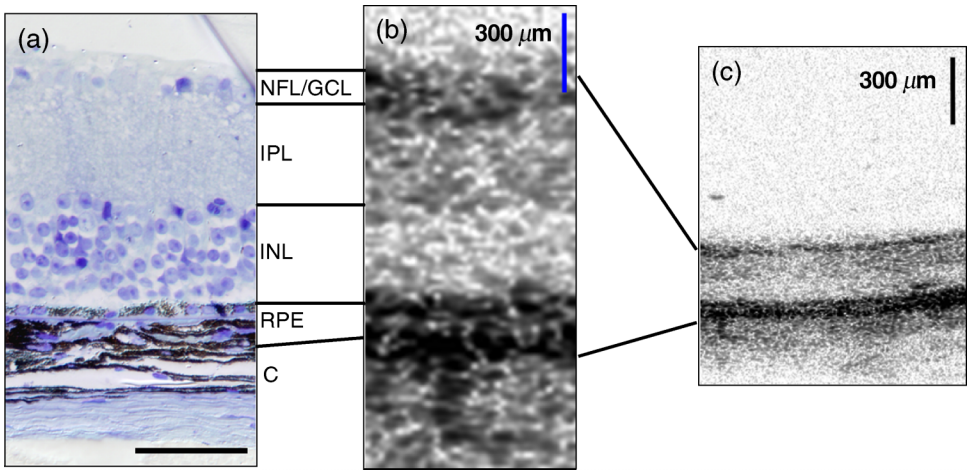

Figure 4. Comparison between a high-resolution SD-OCT image of a rhodopsin knockout mouse retina and a histological image of the same mouse. The SD-OCT image is in good correlation with histology. The scale bar in the histology is 50 μm.

mouse breathing. This movement leads to misalignment among cross-sections and slightly blurs the fundus image. Blood vessels seen in the fundus image cast minimal shadows in the cross-sectional images most likely because they are thin.

Figure 4 compares the SD-OCT image with a histological image from the same mouse. An SD-OCT image strip was resized to match the size of the histological image. Individual retinal layers in the SD-OCT image are identified from the top (proximal) surface of the retina to bottom (distal) as follows: the NFL and GCL (the first dark line), the IPL (the next dark band), and the INL (the next light band). Two strong dark lines on the bottom are identified as the RPE and choroid. Absent in both the SD-OCT and histological images are the outer retinal layers (OPL, ONL, and IS/OS). The histological image shows multiple thin layers close to the RPE and choroid which may account for the darkening of the RPE and choroid lines in the SD-OCT images. These high-resolution SD-OCT images from the rhodopsin knockout mice show microstructures at the end stage of retinal degeneration in good correlation with histology

Monitoring the progression of retinal degeneration in *rd*1 mice

We next monitored the progression of retinal degeneration in *rd*1 mice (C3H/HeJ) by periodically imaging the same mice. We studied *rd*1 mice because their retinal degeneration is both well characterized and rapid (Chang et al., 2002). Their eyes develop normally up to about P7 by which time the outer segments of rods begin to form. After P10 the nascent outer segments and the rod cells rapidly degenerate so that by P15 only a thin layer of rod cells remains. All rod photoreceptors are gone by P35.

A pregnant *rd*1 mouse gave birth to seven pups in our animal facility, and we started high-resolution SD-OCT imaging as soon as the pups opened their eyes spontaneously (P13). We continued imaging the pups twice a week for the next 3 weeks (P34) while sacrificing a mouse per week for histology. A total of four mice were imaged over the entire measurement period. For comparison, we imaged five wild-type pups (C3Sn.BLiA-*Pde6b*$^{+}$/Dn) as sighted controls for the *rd*1 mice.

Using SD-OCT, we detected rapid structural changes in *rd*1 mouse retinas from P13 to P20. Movie 3 presents SD-OCT images of the same retina on P13 (upper image) and

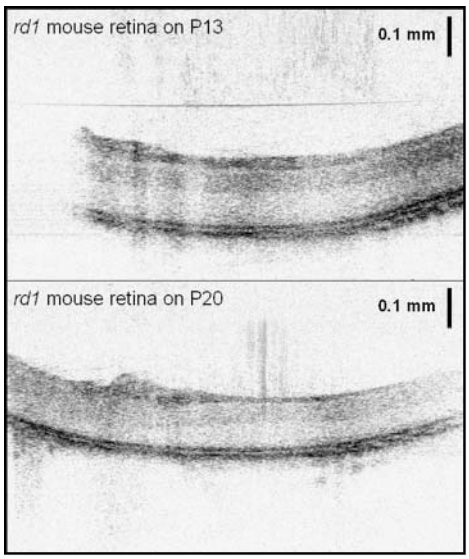

Movie 3. High-resolution SD-OCT images of *rd*1 mouse retina on P13 and P20. On P13, the retina shows fewer layers due to early onset of the degeneration. However, a faint layer band is visible above the RPE in the image on P13. On P20, the retina becomes thinner and the faint band is absent with the degeneration progression.

P20 (lower image). Each cross-sectional image is 1.2 mm × 0.67 mm in the *x*–*z* plane and the cross-section advances with 6 μm steps in the *y* axis. Note that significant degeneration is already evident on P13. The P13 *rd*1 image contains fewer retinal layers than the control. Going from the top (proximal) surface of the retina to bottom (distal), the *rd*1 retina on P13 exhibits a dark line, a dark band, and a light band that may correspond to the NFL + GCL, IPL, and INL, respectively. Below these layers, there are a faint dark line and a narrow light band. Below them, dark lines of the RPE and choroid appear close to the outer surface of the retina. The narrow light band shows uniform thickness throughout the imaged section. The reduced thickness of this retina results primarily from thinning of outer retinal layers that started before P13. The faint dark line and narrow light band are absent in the SD-OCT images taken on P20 and the retina is thinner. Image quality of this movie is not as good as that of the control mouse retina because of shadows caused by a vascular network leading from the optic nerve head to the posterior aspect of the lens. Nevertheless, the movie clearly shows the structural changes that occur in the retina during the early phase of degeneration.

Figure 5 shows SD-OCT retinal images of the same *rd*1 mouse over the entire degeneration phase. For comparison, Figure 5g shows histological images of *rd*1 mice taken at the same time points. Although these histological images were taken from different *rd*1 mice, we assume that their retinas had identical structures as this strain is homozygous for retinal degeneration allele $Pde6b^{rd1}$. Imaging time points were roughly evenly distributed (P13, P20, P23, and P34) during the degeneration phase. Figures 5e and 5f show SD-OCT retinal images of a control mouse (C3Sn.BLiA-$Pde6b^{+}$/Dn). Figure 5g (left) shows a histological image of a control mouse retina taken on P16. The SD-OCT images of the control mouse retina show normal microstructures on P13 (Figure 5e), although individual retinal layers appear in better contrast on P30 (Figure 5f) than on P13. The control mouse retinas have fully developed layered microstructures from the beginning of the longitudinal study on P13 but *rd*1 mouse retinas do not. Captured by SD-OCT imaging, the fewer layers of *rd*1 retinas most likely reflect ongoing degeneration rather than retinal development. The histological image of the *rd*1 mouse at the same time point (P13) confirms the observation in the SD-OCT image: It shows significant reduction in thickness of the outer retina (OPL, ONL, and IS/OS) compared to control mouse retina. The histological image suggests that the faint dark line proximal to the INL in the P13 SD-OCT image corresponds to the OPL and the more distal light narrow band in the SD-OCT image corresponds to the ONL + IS/OS. The ONL and IS/OS layers are not distinguishable in the SD-OCT image on P13, although they appear well resolved in the histological image. This may be because these layers are not as well organized as in the control mouse case and clear boundaries are absent between the layers reducing light back-scattering. On P20, the SD-OCT image shows substantial thinning or a complete absence of the faint dark line and narrow light band, which consists of the OPL, ONL, and IS/OS, in Figure 5b. These layers are not distinguishable even in the histological image on P20 (Figure 5g). The ONL may be absent or extremely thin down to the dimension of a single cell layer. SD-OCT images on P13 and P20 show a large thickness change in the retina between two time points, but this thickness change is not observed in the histological images, which may be due to different contraction ratios of individual retinal layers during histological processing. On P23 (Figure 5c) and P34 (Figure 5d), SD-OCT images show continuous reduction in thickness, although the structural changes are not noticeable. The two dark lines, corresponding to the RPE and choroid, become darker. The histological images show additional multiple layers close to the RPE starting on P20 and becoming prominent on P23 and P34. These layers may be related to the darker lines of the RPE and the choroid in the SD-OCT images. SD-OCT images at later time points show very similar retinal structures to those of the rhodopsin knockout mouse retina shown in Figure 4. Overall, high-resolution SD-OCT imaging shows detailed structural changes in *rd*1 mouse retinas during the degeneration phase and the changes in the SD-OCT images correlate well with the changes in the histological images.

Finally, we analyzed changes in thickness of the *rd*1 mouse retinas during the degeneration phase (Figure 6). In SD-OCT images, length in the axial direction is measured as the path length of light traveling in air. A physical length in a tissue in the axial direction can be calculated by dividing the path length in air with the tissue refractive index. We calculated the thickness of the retina assuming its refractive index to be uniform at 1.4. We measured the thickness of two layers: the outer retina, consisting of the OPL, ONL, and IS/OS, and the whole retina, extending from the NFL to OS (Figures 6b and 6c). 3D images show that retinal thicknesses are relatively uniform except around the optic nerve head where they are thinner. Therefore, for each 3D image we measured retinal thickness at a single location 0.5 mm from the optic nerve head manually. We measured the thicknesses of each retina from two 3D images. On P13, the thickness was measured on 14 *rd*1 retinas, and their average, standard deviation were calculated. Sacrificing mice for histology reduced the number of retinas measured at later time points. On P34, 8 *rd*1 retinas were used for the thickness measurement. Analyses of retinas of both *rd*1 and control mice are shown in Figure 6a.

On P13, the outer retinas of *rd*1 mice are significantly thinner (27 μm) than those of control mice (102 μm). Thickness of the outer retina in *rd*1 mice continues to decrease, reducing to 16 μm on P16 and then to 12 μm on P20. The measurement on P20 was not accurate because

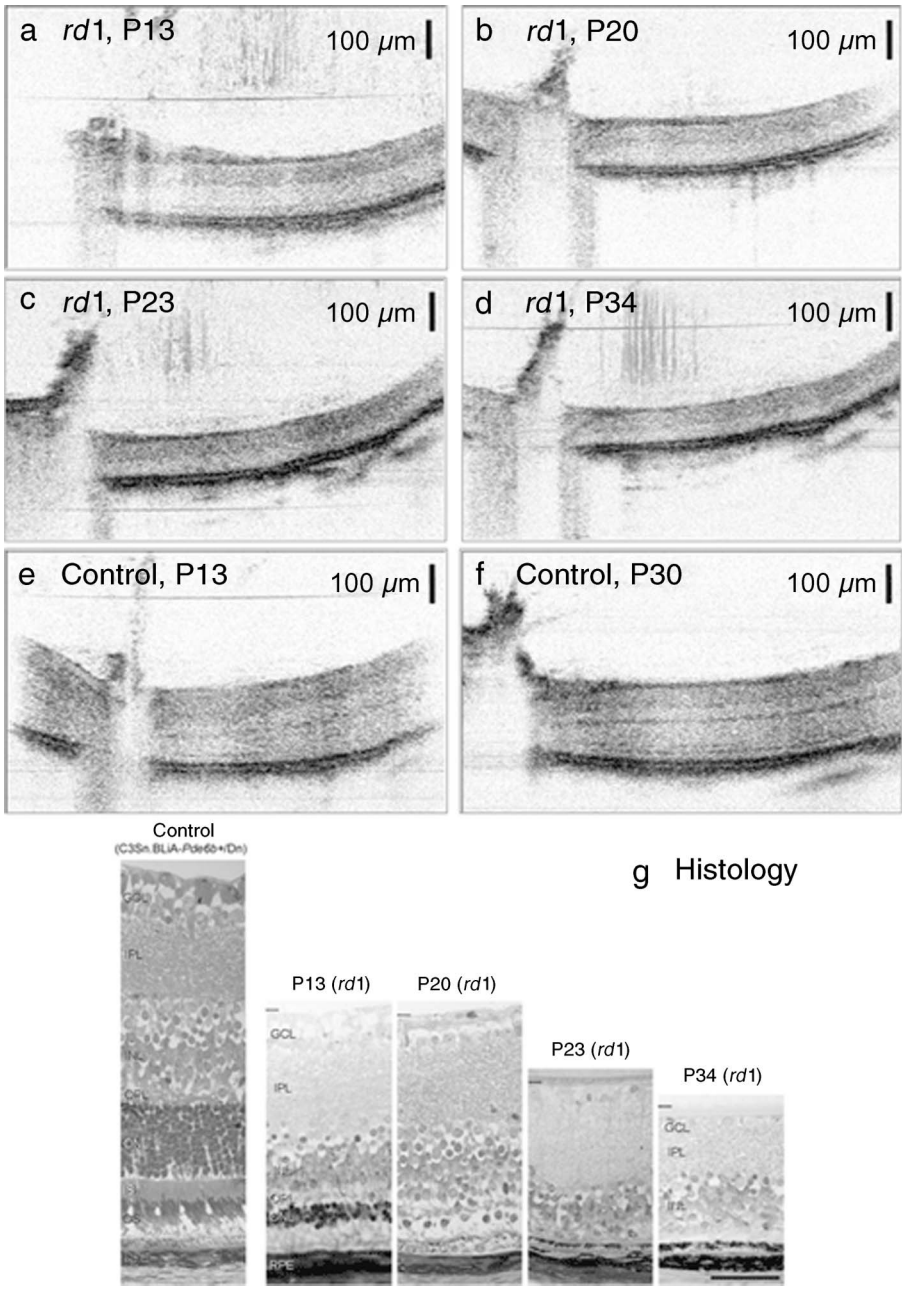

Figure 5. High-resolution SD-OCT images of the same *rd1* mouse retina (a–d) and histological images (g) during the degeneration phase. The same *rd1* mouse retinas were imaged non-invasively in the longitudinal study. Sequential structural changes are observed in the SD-OCT images and confirmed by the histological images. For comparison, high-resolution SD-OCT images of a control mouse retina and a histological image are presented in panels e–f and g, respectively. The images of control mouse retinas show fully developed retinal structures from the beginning of the measurement phase (P13).

the OPL boundaries were not clear. We assumed an exponential decrease in thickness and fitted the P13 and P16 data as shown in Figure 6a. Extrapolation of the fitted curve indicated that the degeneration started approximately on P5. On P13, thickness of whole retina in *rd*1 mice is 150 μm which is significantly smaller than that of control mice (225 μm) and decreases down to less than 100 μm on P34.

Discussion

The high-resolution SD-OCT system is capable of monitoring detailed structural changes in *rd*1 mouse retinas as degeneration progresses. We have performed a longitudinal study of retinal degeneration by imaging retinas of individual *rd*1 mice in vivo from the time of

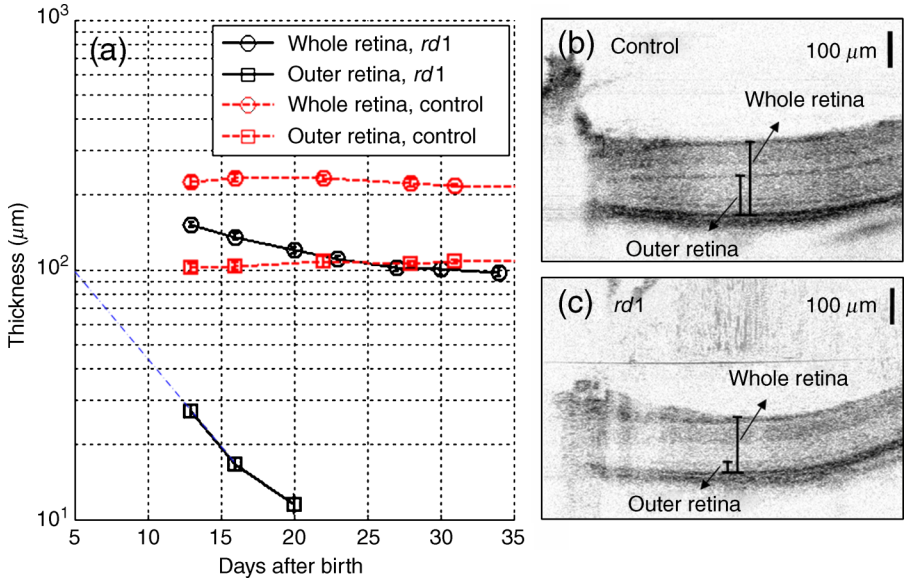

Figure 6. Change in retinal thickness of *rd*1 mouse during the degeneration phase in comparison with control mouse. Measured are the thicknesses of the whole retina from the NFL to OS, and the outer retina composed of the OPL, ONL, and IS/OS as shown in panels b and c. Thickness of the outer retina in *rd*1 mice could be measured only early measurement time points due to the earlier onset of degeneration.

spontaneous eye opening to late stages of degeneration (P13–P34). The OPL, ONL + IS/OS layers were observed on P13, but the individual layers were not distinguishable because of the early onset of degeneration. However, the SD-OCT images of P13 retinas showed their structures in greater detail than was possible in the previous study with a lower-resolution TD-OCT system (Li et al., 2001). Our SD-OCT 3D images of *rd*1 mice also showed that the decreases in retinal thickness progressed uniformly within the 1 mm × 1 mm imaging areas in lateral plane. We found that the high-resolution SD-OCT system could resolve all the major retinal layers in control mice (C57BL/6J, C3Sn.BLiA-*Pde6b*+/Dn) but not with the resolution of standard histological methods. The value of SD-OCT is its capability to image the morphology of the rodent retina non-invasively and thereby to monitor progressive changes caused by degeneration.

For OCT imaging, we applied hydroxypropyl methylcellulose and a coverslip to negate the refractive power of the cornea. This method was beneficial by preventing the eye from dehydration. But we found that the refractive power of the lens degrades the focus of light when scanning in the periphery of the retina. This effect blurs peripheral retinal microstructures of the SD-OCT images with optimal focus limited to the central regions where the IS is discernable in control mice. If necessary, such a lens-induced aberration could be corrected by incorporating adaptive optics (Roorda & Williams, 1999).

High-resolution SD-OCT could measure retinal thickness *in vivo* in the study of *rd*1 mice and thereby avoid potential artifacts of histological processing. We note, however, that thickness measurements are based on the assumption that the retina has constant refractive index of 1.4. More precise thickness measurements would require information on the actual refractive indices of individual retinal layers. However, assuming that their refractive indices do not differ significantly, SD-OCT imaging provides relatively precise thickness information (Srinivasan, Ko, et al., 2006).

Conclusions

A high-resolution SD-OCT system was adapted for non-invasive imaging of the mouse retina. Its depth resolution (less than 3 μm) was adequate for resolving the major layers of the retina. We used the system for tracking the time-dependent degenerative changes in the retinas of individual *rd*1 mice. We found that the outer retina (OPL, ONL, and IS/OS layers) was degenerated with significant thickness reduction (73%) on P13 and was not resolvable by P20. The degeneration progressed with thickness reduction of the retina and reached an asymptotic level by P30–P34. This *rd*1 mouse study demonstrates that high-resolution SD-OCT can monitor the progression of retinal degeneration in transgenic mice.

Acknowledgments

Authors would like to acknowledge Dr. Clint Makino at Massachusetts Eye and Ear Infirmary for providing

rhodopsin knockout mice. This research was supported by NIH grants R01 EY14975 and EY00667 and by Research to Prevent Blindness and the Lions of Central New York.

Commercial relationships: none.
Corresponding author: Johannes F. de Boer.
Email: deboer@helix.mgh.harvard.edu.
Address: 50 Blossom Street, Boston, MA 02114, USA.

References

Alexander, J. J., Umino, Y., Everhart, D., Chang, B., Min, S. H., Li, Q., et al. (2007). Restoration of cone vision in a mouse model of achromatopsia. *Nature Medicine, 13,* 685–687. [PubMed]

Ali, R. R., Sarra, G. M., Stephens, C., Alwis, M. D., Bainbridge, J. W., Munro, P. M., et al. (2000). Restoration of photoreceptor ultrastructure and function in retinal degeneration slow mice by gene therapy. *Nature Genetics, 25,* 306–310. [PubMed] [Article]

American National Standards Institute (2000). *American National Standard for Safe Use of Lasers Z136.1* (No. ANSI Z136.1-2000). Orlando.

Bainbridge, J. W., Tan, M. H., & Ali, R. R. (2006). Gene therapy progress and prospects: The eye. *Gene Therapy, 13,* 1191–1197. [PubMed]

Bowes, C., Li, T., Frankel, W. N., Danciger, M., Coffin, J. M., Applebury, M. L., et al. (1993). Localization of a retroviral element within the rd gene coding for the beta subunit of cGMP phosphodiesterase. *Proceedings of the National Academy of Sciences of the United States of America, 90,* 2955–2959. [PubMed] [Article]

Cense, B., Nassif, N. A., Chen, T. C., Pierce, M. C., Yun, S.-H., Park, B. H., et al. (2004). Ultrahigh-resolution high-speed retinal imaging using spectral-domain optical coherence tomography. *Optics Express, 12,* 2435–2447. [Article]

Chang, B., Hawes, N. L., Hurd, R. E., Davisson, M. T., Nusinowitz, S., & Heckenlively, J. R. (2002). Retinal degeneration mutants in the mouse. *Vision Research, 42,* 517–525. [PubMed]

de Boer, J. F., Cense, B., Park, B. H., Pierce, M. C., Tearney, G. J., & Bouma, B. E. (2003). Improved signal-to-noise retio in spectral-domain compared with time-domain optical coherence tomography. *Optics Letters, 28,* 2067–2069.

Drexler, W., Morgner, U., Ghanta, R. K., Kärtner, F. X., Schuman, J. S., & Fujimoto, J. G. (2001). Ultrahigh-resolution ophthalmic optical coherence tomography. *Nature Medicine, 7,* 502–507. [PubMed] [Article]

Fercher, A. F., Hitzenberger, C. K., Kamp, G., & El-Zaiat, S. Y. (1995). Measurement of intraocular distances by backscattering spectral interferometry. *Optics Communication, 117,* 43–48.

Fujimoto, J. G. (2003). Optical coherence tomography for ultrahigh resolution in vivo imaging. *Nature Biotechnology, 21,* 1361–1367. [PubMed]

Gloesmann, M., Hermann, B., Schubert, C., Sattmann, H., Ahnelt, P. K., & Drexler, W. (2003). Histologic correlation of pig retina radial stratification with ultrahigh-resolution optical coherence tomography. *Investigative Ophthalmology & Visual Science, 44,* 1696–1703. [PubMed] [Article]

Hausler, G., & Lindner, M. W. (1998). "Coherence radar" and "spectral radar"—New tools for dermatological diagnosis. *Journal of Biomedical Optics, 3,* 21–31.

Hauswirth, W. W., & Beaufrere, L. (2000). Ocular gene therapy: Quo vadis? *Investigative Ophthalmology & Visual Science, 41,* 2821–2826. [PubMed] [Article]

Horio, N., Kachi, S., Hori, K., Okamoto, Y., Yamamoto, E., Terasaki, H., et al. (2001). Progressive change of optical coherence tomography scans in retinal degeneration slow mice. *Archives of Ophthalmology, 119,* 1329–1332. [PubMed]

Huang, D., Swanson, E. A., Lin, C. P., Schuman, J. S., Stinson, W. G., Chang, W., et al. (1991). Optical coherence tomography. *Science, 254,* 1178–1181. [PubMed]

Leitgeb, R., Hitzenberger, C. K., & Fercher, A. F. (2003). Performance of Fourier domain vs. time domain optical coherence tomography. *Optics Express, 11,* 889–894. [Article]

Lem, J., Krasnoperova, N. V., Calvert, P. D., Kosaras, B., Cameron, D. A., Nicolò, M., et al. (1999). Morphological, physiological, and biochemical changes in rhodopsin knockout mice. *Proceedings of the National Academy of Sciences of the United States of America, 96,* 736–741. [PubMed] [Article]

Li, Q., Timmers, A. M., Hunter, K., Gonzalez-Pola, C., Lewin, A. S., Reitze, D. H., et al. (2001). Noninvasive imaging by optical coherence tomography to monitor retinal degeneration in the mouse. *Investigative Ophthalmology & Visual Science, 42,* 2981–2989. [PubMed] [Article]

Morgan, J., Huckfeldt, R., & Wong, R. O. (2005). Imaging techniques in retinal research. *Experimental Eye Research, 80,* 297–306. [PubMed]

Nassif, N., Cense, B., Park, B. H., Yun, S. H., Chen, T. C., Bouma, B. E., et al. (2004). In vivo human retinal imaging by ultrahigh-speed spectral domain optical coherence tomography. *Optics Letters, 29,* 480–482.

Otani, A., Dorrell, M. I., Kinder, K., Moreno, S. K., Nusinowitz, S., Banin, E., et al. (2004). Rescue of retinal degeneration by intravitreally injected adult bone marrow-derived lineage-negative hematopoietic

stem cells. *Journal of Clinical Investigation, 114,* 765–774. [PubMed] [Article]

Roorda, A., & Williams, D. R. (1999). The arrangement of the three cone classes in the living human eye. *Nature, 397,* 520–522. [PubMed]

Ruggeri, M., Wehbe, H., Jiao, S., Gregori, G., Jockovich, M. E., Hackam, A., et al. (2007). In vivo three-dimensional high-resolution imaging of rodent retina with spectral-domain optical coherence tomography. *Investigative Ophthalmology & Visual Science, 48,* 1808–1814. [PubMed]

Srinivasan, V. J., Ko, T. H., Wojtkowski, M., Carvalho, M., Clermont, A., Bursell, S. E., et al. (2006). Noninvasive volumetric imaging and morphometry of the rodent retina with high-speed, ultrahigh-resolution optical coherence tomography. *Investigative Ophthalmology & Visual Science, 47,* 5522–5528. [PubMed]

Srinivasan, V. J., Wojtkowski, M., Fujimoto, J. G., & Duker, J. S. (2006). In vivo measurement of retinal physiology with high-speed ultrahigh-resolution optical coherence tomography. *Optics Letters, 31,* 2308–2310.

Swanson, E. A., Huang, D., Hee, M. R., Fujimoto, J. G., Lin, C. P., & Puliafito, C. A. (1992). High-speed optical coherence domain reflectometry. *Optics Letters, 17,* 151–153.

Wojtkowski, M., Leitgeb, R., Kowalczyk, A., Bajraszewski, T., & Fercher, A. F. (2002). In vivo human retinal imaging by Fourier domain optical coherence tomography. *Journal of Biomedical Optics, 7,* 457–463. [PubMed]

Wojtkowski, M., Srinivasan, V. J., Ko, T. H., Fujimoto, J. G., Kowalczyk, A., & Duker, J. S. (2004). Ultrahigh-resolution, high-speed, Fourier domain optical coherence tomography and methods for dispersion compensation. *Optics Express, 12,* 2404–2422. [Article]